Stokes shift microscopy by excitation and emission imaging

Krause, S.; Vosch, T.

Stokes shift microscopy by excitation and emission imaging

S. KRAUSE[1,2] AND T. VOSCH[1,3]

[1]*Nano-Science Center/Department of Chemistry, University of Copenhagen Universitetsparken 5, 2100 Copenhagen, Denmark*
[2]*stefan.krause@chem.ku.dk*
[3]*tom@chem.ku.dk*

Abstract: In this contribution, we present a new method, based on a tunable excitation laser source and a robust common path interferometer in the detection channel. Its purpose is to image spectral excitation and emission information on a monochrome complementary metal oxide semiconductor (CMOS) camera. This allows us to spatially obtain both excitation and emission spectra of the whole imaged area and create derived images such as red-green-blue (RGB), excitation and emission maxima, and Stokes shift images. Our presented method is a further development of hyperspectral imaging that usually is limited to recording spatially resolved emission spectra. Taking advantage of the full camera chip should speed up the acquisition versus line scan or pointwise hyperspectral imaging.

1. Introduction

Applications of fluorescence spectroscopy in life and materials science are wide spread [1,2]. Non-invasiveness, ease to implement, and specificity are only a few of the many advantages provided by fluorescence spectroscopy. By combining fluorescence methods with microscopy, one can obtain diffraction limited spatial information, which allows probing heterogeneities of micro- and nanostructures. One of such approaches involves measuring spatially resolved spectral information [3–5]. This so called hyperspectral imaging approach has promoted fundamental progress for the investigation of various samples e.g. cells [6–12], chromosomes [13,14], organic tissue [15–18], or nanomaterials [19–21]. While measuring spatially resolved emission spectra has become relativity standard in many laboratories, measuring excitation spectra is more challenging since it requires a tunable excitation source or an interferometer in the excitation path [22,23]. Examples of combining emission and excitation spectroscopy simultaneously are even scarcer [24–26]. Here we demonstrate that emission-side interferometry, in combination with a tunable excitation light source, offers an opportunity to achieve spatially resolved excitation and emission information in wide field or TIRF configuration [6].

For recording the spatially resolved emission spectra, we rely on a robust and ultra-stable interferometer that is based on birefringent materials, creating a polarization based time delay between two beams travelling on a common path [27–29]. The advantage of this approach is that the interferometer does not require beam stabilization or precise beam alignment. We have recently shown that implementation of such an interferometer in the excitation path of a confocal microscope allows recording excitation spectra of single molecules [29]. In that case the interferometer is solely modulating the broadband excitation light and the excitation and emission information are recorded from a single spot in a confocal manner. However, the application of the common path interferometer in the detection path of a widefield microscope is different and more versatile since it allows transmitting the spatially resolved spectral information of a large area at once. For recording the spatially resolved excitation spectra, we use a continuum laser source with an acousto-optic tunable filter (AOTF) wavelength selector. Scanning the excitation wavelength and simultaneously acquiring the

emission intensity allows us to reconstruct the spatially resolved excitation spectrum of the specimen. This approach yields images with full spectral (excitation and emission) information with a monochromatic camera. Moreover, it can be applied to samples of high spatial density since it does not demand distinguishable spots, commonly required for line-based hyperspectral imaging with diffraction gratings or prisms [8,30,31].

We demonstrate our excitation/emission imaging (EEI) approach with a mixture of seven different dye-coated zeolite crystals and compare the results with dispersion-based reference spectra. Additionally, we show, for a polarity sensitive dye, the spectral variations in excitation and emission, induced by differences in the matrix polarity.

2. Results and discussion

The experimental setup is shown in Fig. 1(a) and consists of scientific grade microscopy components in combination with a tunable light source and a common path interferometer in the detection path. Thereby, excitation spectroscopy is performed by scanning the laser line of a continuum white light laser and collecting the red-shifted fluorescence signal with a camera (see Fig. 1(b)). In addition, emission spectra are obtained by placing a birefringent based interferometer [32,33] in front of the complementary metal oxide semiconductor (CMOS) camera. For ideal polarization of the entrance light, the interferometer throughput is close to 100% and therefore higher than for standard dispersion based spectrographs. The interferometer introduces a tunable delay between s- and p- polarization component of the fluorescence light. For each position of the interferometer, the fluorescence signal is detected on the CMOS camera. The time series of images provides an interferogram at each pixel which corresponds to the Fourier transform of the emission spectrum (see Fig. 1(c)). This approach allows for a fast acquisition of spatially resolved excitation and emission spectra of a large area. Assuming 0.5 s integration time per frame while scanning from 450 nm to 620 nm in steps of 2 nm results in an acquisition time of 42.5 s. A similar time of 40 s is needed for measuring a spatially resolved interferogram with 200 data points and 0.2 s integration time per frame. This gives an overall measurement time of 82.5 s which can be further reduced by an appropriate choice of polarization optics and a high-power laser source. The advantage here is the parallel acquisition of data over the whole region of interest typically consisting of about 500 by 500 pixels. Performing the same experiment with a scanning confocal microscope leads to extremely long acquisition times. We can estimate the acquisition of a single excitation spectrum to be faster since the excitation intensity is strongly increased. The applied laser poses a technical limit of about 50 ms per data point which gives 4.25 s per excitation spectrum. Also, a single emission spectrum would require less integration time which we estimate to be in the best case in the range of 0.01 s. However, the major drawback here is the scanning of a large number of pixels. This gives a total measurement time of $500 \times 500 \times 4.26$ s $= 295.6$ h which is unrealistic for an experiment. Reducing the pixel number would increase the acquisition speed but also reduce the image quality. At such long exposure times it is likely that thermal drift would lead to image distortions.
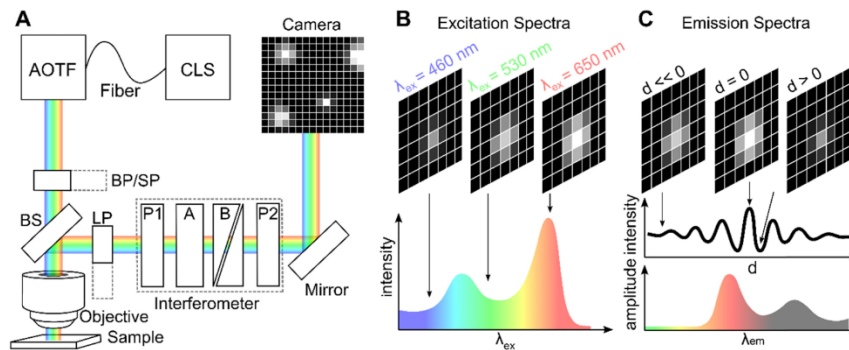
Fig. 1. A) Scheme of the experimental setup consisting of a continuum light source (CLS), fiber, acousto-optic tunable filter (AOTF), beam splitter (BS), band pass (BP), short pass (SP) and long pass (LP) filters, objective, sample, birefringent wedge interferometer with polarizers (P1 & P2), birefringent block A and birefringent wedges B, mirror and a CMOS camera [27,32,33]. B) Measurement procedure for excitation spectra based on scanning the excitation wavelength. C) Measurement procedure for emission spectra based on interference of the fluorescence emission which leads to destructive/constructive interference depending on the optical path difference d and the transmitted spectrum. The Fourier transform yields the emission spectrum at every pixel.

2.1 Hyperspectral imaging of seven different dyes

To test the presented EEI setup and verify its performance, we produced a heterogeneous sample of dye-coated zeolite 5A crystals as described in the materials and methods section. These samples are ideal for demonstrating purposes as they feature bright emission from spatially well separated crystals which differ strongly in absorption and emission properties. Each crystal was coated with one of seven possible dyes. A 60 x 60 μm^2 region of such a sample is shown in the light transmission image in Fig. 2(a). The crystals are randomly distributed and, in most cases, spatially separated. Despite the fact that we chose seven different dyes based on their solution spectral properties, coating the dyes on the zeolite crystals led to spectral changes which resulted in the fact that Rhodamine B became indistinguishable from Alexa 546 (see Fig. 5). The same also happened for Rhodamine 101 and Alexa 594 (see Fig. 5). Dyes with overlapping excitation and emission spectra will always be hard to discriminate from each other with any spectrally resolving technique. If necessary, other parameters like decay time or anisotropy might be useful tools for discrimination. However, for the spectral imaging demonstration here, this is not a problem; it only means that we cannot discriminate with absolute certainty Rhodamine B from Alexa 546 and Rhodamine 101 from Alexa 594. We acquired the fluorescence emission of this sample area upon 473 nm excitation while scanning the common path interferometer at the same time from about −0.6 mm to 0.6 mm. This wavelength was chosen since it was capable of exciting all seven dyes at varying levels of efficiency. The sum of the recorded intensity of all frames is shown in Fig. 2(b). It resembles the transmission image and verifies that all crystals are fluorescent. The resulting interferograms (examples shown in Fig. 2(e)) at each pixel were then Fourier transformed to obtain the full emission spectrum with a line width resolution of 50 nm at 550 nm – which is sufficient for the broad dye spectra - and a peak positioning accuracy of about 0.3 nm for the highest signal-to-noise ratio [34,35]. This spectral information can now be used to create different types of images or be used for spectral unmixing which is, however, beyond the scope of this experimental methods article [5]. For demonstration purposes Fig. 2(d) shows an emission maximum image, color-coded according to the scalebar. The intensity matrix shown in Fig. 2(b) in combination with a fixed threshold serves as a mask in Fig. 2(d) in order to exclude non-zeolite related regions, which can be considered as background in this case. Representative spectra of the marked spots are displayed in Fig. 2(e) together with the corresponding interferograms.
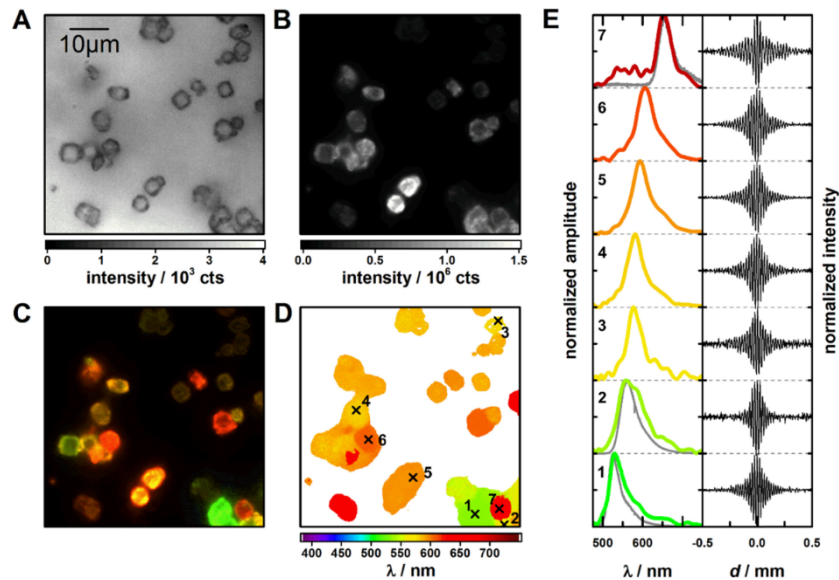
Fig. 2. A) Transmission image of dye-doped zeolite crystals. B) Integrated fluorescence intensity from the interferometric data. C) Reconstructed RGB image from the spectra of each pixel. D) Color-coded emission maximum image. Values below a certain intensity threshold are colored white. The pixel size corresponds to 115 nm. E) Example spectra and interferograms of the marked spots in D. The gray spectra have been acquired confocally with a dispersion-based spectrograph from samples of unmixed zeolite crystals (see Fig. 5). Spot 1 can be associated with Atto 488, spot 2 with Rhodamine 6G, spot 7 with Atto 633.

We associated the emission spectra at each pixel with a red (R), green (G) and blue (B) wavelength range to create an RGB image in Fig. 2(c) as explained in more detail in the materials and methods section and Fig. 7. Emission maxima, as well as the RGB image, allow for an easy assessment of the different dye coated zeolites. However, while the RGB image suggests, e.g. that the emission properties at spot 6 and 7 are very similar, the emission spectra show that both particles are coated with different dyes. Association of spectral features to individual dyes was done by comparing the recorded spectra to reference spectra of the unmixed dye coated zeolites (see gray spectra in Fig. 2(e) and Fig. 5). While the association is unambiguous for Atto 488, Rhodamine 6G and Atto 633, two pairs of dye coated zeolites cannot be discriminated from each other, as pointed out previously. Apart from creating RGB images and plotting of peak positions, any other image can be created with the gained spectral information at each pixel. This includes FWHM information as well as ratio metric imaging.

2.2 EEI of four spectrally close lying dyes

The spatially resolved excitation spectrum can be measured by applying a tunable light source – in our case a continuum laser equipped with an AOTF. The fluorescence emission is then recorded while continuously scanning the excitation wavelength. For this purpose, the interferometer is set to zero delay in order to allow for maximum transmission. While scanning the full visible excitation range (420 nm to 700 nm) is technically possible, it is not advisable since it requires a 700 nm long pass filter which would suppress most of the fluorescence from blue and green emitters. Therefore, multiple scans with a shorter excitation range (e.g. 100 nm) and appropriate long pass filters are preferable. For demonstrating purposes, and in order to capture the excitation spectra in one scan, we have chosen four spectrally close lying dyes: Rhodamine 6G (530/560), Alexa 546 (555/575), Rhodamine B (557/577) and Alexa 594 (580/605). Transmission and integrated fluorescence images of such

a sample are shown in Figs. 3(a) and 3(d). Individually dye coated zeolite crystals are again clearly visible in the transmission and integrated fluorescence image. Measuring the excitation spectrum at every single pixel of the image has been performed by scanning the excitation wavelength from 450 nm to 620 nm in steps of 2 nm at a scanning speed of 500 ms per step, using a 633 nm LP filter in front of the CMOS camera. Faster scan rates for both, excitation and emission, are possible but in the present work inhibited by the low available excitation intensity of less than 10 W/cm^2. Fluorescence images were recorded simultaneously. After correction for the wavelength dependent laser intensity, we receive excitation spectra such as the spectra exemplarily shown in Fig. 3(g) at every single pixel. For plotting maximum excitation and emission images as shown in Figs. 3(e) and 3(f), the product of the excitation and emission intensity matrix was combined with a fixed threshold in order to color non-zeolite related regions (background) white. The depicted excitation spectra have been taken from individual zeolites, marked in Figs. 3(e), 3(f), and 3(h) and resemble the four different dyes which have been used to coat the zeolite crystals. We find excitation peak positions at about 530 nm (Rhodamine 6G), 560 nm (Rhodamine B and Alexa 546) and 580 nm (Alexa 594). Again, no clear decision can be drawn whether spectra peaking at about 560 nm belong to Rhodamine B or Alexa 546 or even result from overlapping dye species (see for example spectrum 5 in Fig. 3(g)). The overlapping can be due to cross-contamination upon mixing or due to overlapping zeolite particles in the same area. However, combining excitation and emission information does allow us to extract information about the distinguishable dyes at most locations. Exciting at 473 nm and using the common path interferometer in front of the CMOS camera will give us the emission spectra, while the excitation scan of the continuum laser will give us the excitation spectrum at every pixel, as shown in Fig. 3(g). Spot 3 and 5 can now be easily distinguished from each other by the different emission spectra and Stokes shift. Spot 3 belongs to Rhodamine B or Alexa546 (which cannot be distinguished, neither by excitation nor emission spectra, see Fig. 5) while spot 5 can be attributed to Alexa594 overlapping with Rhodamine B or Alexa546 (see Fig. 5). At this point an experimental validation of the gained spectra through comparison with conventional fluorescence measurements of the dye in solution is not appropriate since the spectral properties of the dyes attached to zeolite crystals deviate strongly from the solvent case. In order to verify the accuracy of the interferometer-based emission spectra, we measured at the same positions the emission spectra with a confocal microscope equipped with a dispersion-based spectrometer. The resulting spectra are shown in Fig. 3(g) in green and agree well with the spectra we received from the interferometer approach. Slight deviations might arise from the smaller excitation volume of the confocal microscope in comparison to the widefield microscope. The excitation and emission spectra were again used to create RGB images and can be seen in Figs. 3(b) and 3(c). The difference in peak positions for excitation and emission contained in Figs. 3(e) and 3(f) yield the spatially resolved Stokes shift presented in Fig. 3(h). Combined excitation, emission and Stokes shift images allow us to identify spots stained with the same dye (spot 3 and 4) as well as to distinguish between different dyes which appear similar, e.g. in emission (spot 2 and 3).
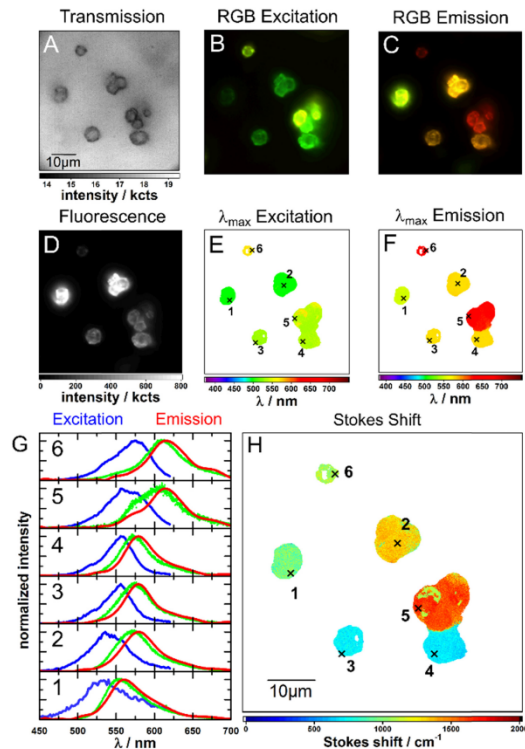
Fig. 3. A) Transmission image of dye-doped zeolite crystals. B) Reconstructed RGB image from the excitation spectra at each pixel. C) Reconstructed RGB image from the Fourier transform of the interferogram at each pixel. D) Integrated fluorescence intensity from the interferometric data. E) Color-coded excitation maximum image. Values below a certain intensity threshold are colored white. F) Color-coded emission maximum image. Values below a certain intensity threshold are colored white. The pixel size corresponds to 115 nm. G) Example excitation and emission spectra of the marked spots in Figs. 3(e) and 3(f). For comparison, the emission spectra recorded at the same positions with a confocal microscope and a dispersion-based spectrograph are shown in green (see spectra of the unmixed dye coated zeolites in Fig. 5) H) Color-coded Stokes shift in units of cm^{-1} as calculated from the excitation and emission maxima from the data in Figs. 3(e) and 3(f). Values below a certain intensity threshold are colored white.

2.3 Stokes shift imaging of a polarity sensitive dye

The previous example demonstrates how imaging spatially resolved excitation, emission maxima and Stokes shifts can help to distinguish between different emissive features. In a next example, we want to use Stokes shift imaging in order to determine different polymers (polarity), containing Nile Red that coat zeolite 5A crystals. Nile Red has been widely used as a molecular probe for polarity in lipids [36–39] and polymers [40]. Individual batches of Nile Red embedded in PVA or PEG attached to zeolite crystals were mixed and deposited on a coverslip. Similar to our previous examples the zeolite crystals act as a support to form heterogeneous micrometer sized structures. Fluorescence excitation spectra were acquired by scanning the excitation wavelength from 450 to 640 nm in steps of 1 nm and simultaneously measuring the fluorescence emission after being transmitted through a 647 nm long pass filter. The measured fluorescence intensity values were corrected afterwards for the wavelength dependent laser intensity. The interferograms were acquired at 473 nm excitation wavelength by scanning the common path interferometer from −0.5 mm to 0.5 mm within 200 steps using a 488 nm long pass filter. Figure 4 shows transmission, integrated fluorescence, RGB images and color-coded maxima for excitation and emission as well as the

Stokes shift images together with example spectra of five different spots. The influence of the two different polymers on the excitation and emission properties are obvious when comparing the five different example spots. Spot 1 and 2 with excitation maxima at about 560 nm and emission maxima at about 630 nm can be clearly attributed to Nile Red embedded in PEG when compared with the ensemble data of a pure Nile Red/PEG polymer film (see Fig. 6). Contrary, spot 3, 4 and 5 can be associated with emission from Nile Red being embedded in PVA with excitation maxima at about 595 nm and emission maxima at about 610 nm (see Fig. 6). Inspection of Figs. 4(c) and 4(f) reveal only minor changes for emission spectra of Nile Red in the two polymers. Emission spectra are commonly used as a measure for polar or hydrophobic heterogeneities in life and materials sciences [12,36,39]. Therefore, accurate spatial discrimination of such heterogeneities might be hampered when environmental effects on the emission properties become negligible. Simultaneous acquisition of spatially resolved excitation spectra can provide additional means to probe these heterogeneities as can be seen from Figs. 4(b), 4(e), and 4(h). For the present example the spatial distribution of the Stokes shift in Fig. 4(h) gives the best contrast and allows for an easy and visually intuitive discrimination of the two different polymers.
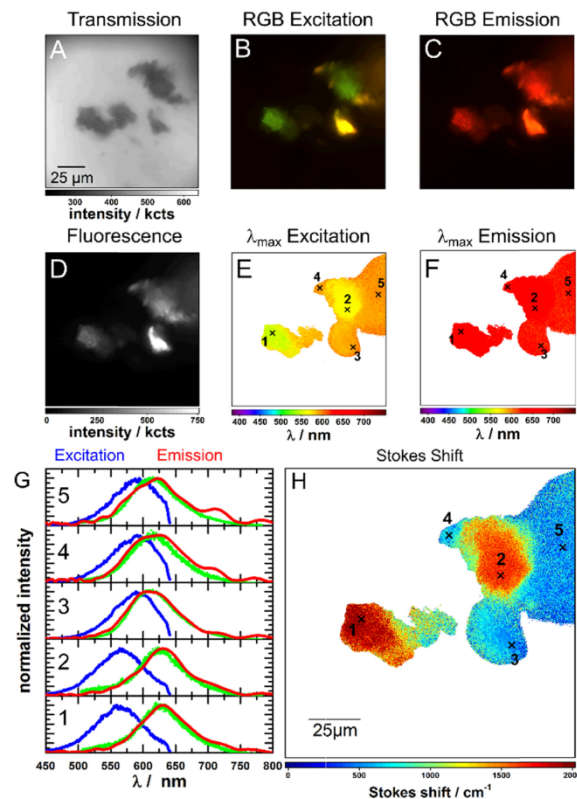

Fig. 4. A) Transmission image of Nile Red doped PVA and PEG coated zeolite crystals. B) Reconstructed RGB image from the excitation spectra at each pixel. C) Reconstructed RGB image from the Fourier transform of the interferogram at each pixel. D) Integrated fluorescence intensity from the interferometric data. E) Color-coded excitation maxima image. Values below a certain intensity threshold are colored white. F) Color-coded emission maximum image. Values below a certain intensity threshold are colored white. The pixel size corresponds to 287 nm. G) Example excitation and emission spectra of the marked spots in Figs. 4(e) and 4(f). For comparison, the emission spectra recorded at the same positions with a confocal microscope and a spectrograph are shown in green. H) Color-coded Stokes shift in units of cm^{-1} as calculated from the difference between the data in Figs. 4(e) and 4(f). Values below a certain intensity threshold are colored white.

3. Materials and methods

The experimental setup is shown in Fig. 1(a) and consists of scientific grade microscopy components (inverted microscope, objective, filters, CMOS camera) in combination with a tunable light source (continuum laser with an AOTF) and a common path interferometer in the detection path.

Excitation spectroscopy was performed by scanning the laser line of a continuum white light laser (NKT SuperK EXTREME EXB-6 with SuperK SELECT AOTF wavelength selector). The SuperK SELECT provides a laser line width of about 3.5 nm full width at half maximum [41]. Remaining laser sidebands were cleaned up with a 633 nm or 650 nm short pass filter (SP01-633RU-25 and FF01-650/SP-25, Semrock). The laser light was then reflected by a 30:70 beam splitter (XF122 Omega Optical) into an Olympus IX71 microscope and illuminated the sample through an objective (Olympus, UPLFLN 100 × NA = 1.4, PLAN FL N 100 × NA = 0.95 or PlanC N 40 × NA = 0.65). The red-shifted fluorescence signal was collected by the same objective. Afterward, the remaining laser light was blocked by a 633 nm (BLP01-633R-25, Semrock) or 647 nm (BLP01-647R-25, Semrock) long pass filter. The excitation wavelength was scanned in steps of 1 or 2 nm while the fluorescence signal was acquired with a CMOS camera (Hamamatsu ORCA-flash 4.0 C11440) for each excitation step (see Fig. 1(b)). Excitation power correction of all measurements was performed by measuring the power above the objective as a function of excitation wavelength with a photodiode power sensor (S120VC Thorlabs).

Confocal microscopy for comparing the Fourier based emission spectra with dispersion-based emission spectra was performed using a home-built confocal microscope. Details on this setup can be found in work from Liao et al. [42]. Confocal excitation spectra were recorded the same way as described above by scanning the laser line of a continuum white light laser, now using only an avalanche photo diode (Perkin-Elmer CD3226) as detector.

Emission spectra were obtained by placing a birefringent based interferometer (GEMINI, NIREOS) [32,33] in front of the CMOS camera. The interferometer firstly polarizes the emission linearly by a Glan-Thompson prism at an angle of 45° with respect to the fast axis of the following birefringent block A (see Fig. 1(a)). This block A introduces a fixed delay between the two orthogonal components of the beam. Block B consists of two identical birefringent wedges with the opposite orientation of the fast and slow optical axis with respect to block A. One of the wedges is mounted on a precision translational stage which allows for tuning the position of the wedge and thereby the effective optical path length in the birefringent material of block B. Typically, the displacement between the two wedges of the interferometer was scanned from −0.5 mm to 0.5 mm within 200 steps (resulting in a wavelength accuracy of about 0.3 nm for the maximum achievable signal-to-noise ratio). For each step of the interferometer, the fluorescence signal was detected on the CMOS camera. The time series of images provides an interferogram at each pixel which corresponds to the Fourier transform of the emission spectrum (see Fig. 1(c)). However, since the time delay of the two beam paths is not linearly dependent of the wedge position, the interferometer needs to be calibrated with back reflected white light and a spectrograph with an optical fiber whose entrance is placed in the imaging plane where otherwise the camera is positioned. A detailed description of how the calibration process works can be found in a recent publications from Perri et al. [27]. Synchronization of the continuum laser, interferometer, and CMOS camera was accomplished by self-written LabVIEW routines. Data analysis was performed with self-written MATLAB routines.

3.1 Sample preparation

In order to obtain micro particles with different excitation and emission maxima we prepared seven batches of 10 mg zeolite 5A (zeolites are a gift from UOP Antwerpen), each coated with one of seven different commercial dyes at high concentration (ATTO 488 – ATTO-TEC,

Rhodamine 101 - Merck, Alexa 546 – Invitrogen, Rhodamine 6G - Merck, Rhodamine B - Merck, Alexa 594 – Invitrogen and ATTO 633 – ATTO-TEC). After evaporation of the solvent, the surface dyed zeolite crystals were mixed and spread on a cover glass in order to image the bright crystals, each with an individual dye coating. Reference spectra can be found in Fig. 5. During the mixing process the differently coated zeolites can come in contact with each other allowing for cross-contamination to a certain extend.
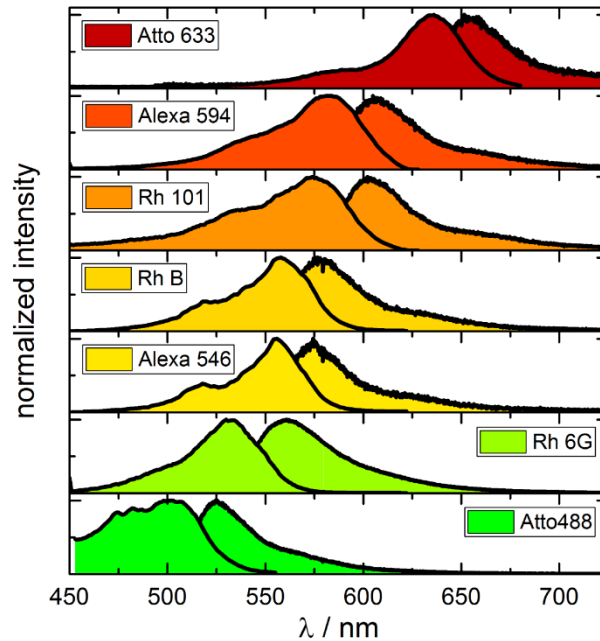

Fig. 5. Confocally measured excitation and emission spectra from non-mixed dye coated zeolite crystals utilized also for the experiment shown in Fig. 2. Excitation wavelength for acquiring emission spectra was 473 nm.

In order to prepare heterogeneous samples with the polarity sensitive fluorophore, we prepared an aqueous solution of poly vinyl alcohol (PVA - Merck) and another aqueous solution with poly ethylene glycol (PEG – Sigma Aldrich/Merck). After adding Nile Red (Thermo Fisher Scientific) to both solutions, the zeolite 5A crystals were added to the individual solutions. After solvent evaporation the crystals, coated with the different Nile Red-embedding polymers, were mixed and spread on a cover glass. Reference spectra can be found in Fig. 6.
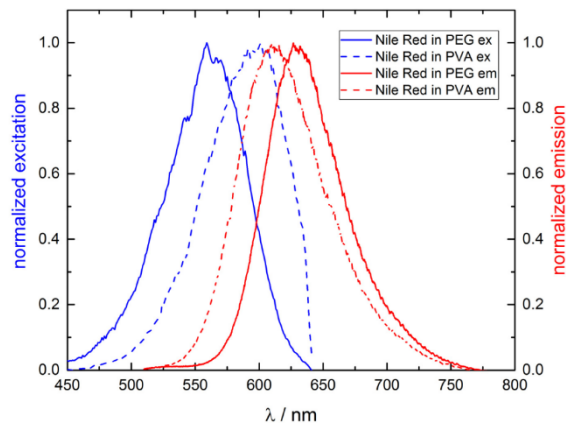
Fig. 6. Confocally measured excitation (blue) and emission (red) spectra of Nile Red embedded in films of pure PVA (solid, Stokes shift 336 cm^{-1}) and pure PEG (dashed, Stokes shift 1855 cm^1).

3.2 Image creation

The spectral regions for R, G and B are color-coded in Fig. 7(a) and have been defined arbitrarily as B = 420 - 498.5 nm, G = 498.5 – 576 nm and R = 576 - 750 nm. The RGB images are created by associating the highest intensity which can be found with respect to pixels and RGB channels to the number 255. In this case, the red channel at position 1 gives the highest intensity with 10.72 Mio. cts. Hence, the green and blue channel at position 1 are associated with the values 3.75 / 10.72 · 255 = 89 and 0.3 / 10.72 · 255 = 7, respectively. We analyze the data of all other pixels the same way, always referring to 10.72 Mio. cts as the reference value for normalization. Superimposing the resulting RGB values results in the RGB image as shown in Fig. 2(c) and Fig. 7(b) on the left side. The RGB values together with the color are additionally shown in Fig. 7(c) for the three example positions. Apparently, the RGB colors for position 1 and 2 differ dramatically despite the fact that the spectra differ only in intensity. From this we can conclude that RGB colors are not an ideal measure for spectral features since they are intensity dependent. This becomes even more obvious, when simply multiplying the RGB values by a factor of 3 and in this case saturating some of the color detection channels. The resulting RGB image in the middle of Fig. 7(b) appears brighter but the colors as depicted for the three example positions in Fig. 7(c) have not much in common with the previous RGB colors. A more representative option for visualizing spectral properties constitutes color-coded plotting of the peak positions, especially in case of emitters featuring well-defined emission spectra. An example of such a plot can be found in Fig. 7(b) on the right side where the color-coded wavelength of the emission maximum of each pixel is plotted. Since position 1 and 2 belong to the same particle, hence dye, the spectral properties are the same and the plot shows the same color for both positions.
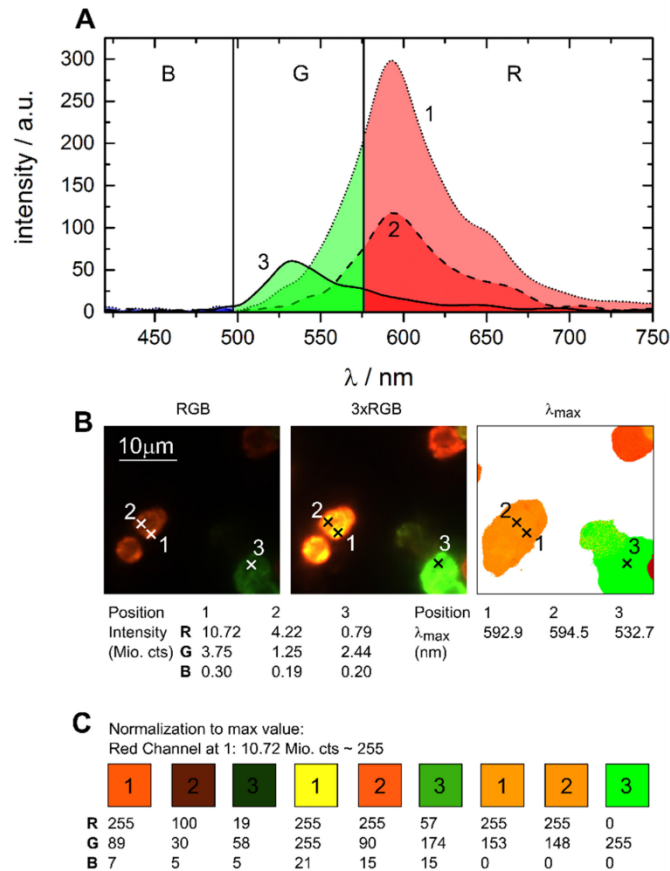
Fig. 7. A) Representative emission spectra of the three spots marked in B after Fourier transformation. The three areas mark the color channels for red, green and blue. B) Left: RGB image reconstructed from the emission intensity values appearing in the R, G and B channel for all pixels. Middle: Same as left but with threefold increased RGB values. Right: Image of the emission maximum wavelength for every pixel. The wavelength values have been converted to RGB values in order to plot them correctly. Values below a certain intensity threshold are colored white. Also shown are the intensity values for the example positions 1, 2 and 3 with respect to the RGB channels. C) Color examples for position 1, 2 and 3 for the three cases shown in B including the applied RGB values.

4. Conclusions

We have introduced a setup that allows for spatially resolved excitation and emission imaging (EEI) based on a tunable continuum light source and a common path interferometer in the detection path. The ease of implementation of the common path interferometer facilitates the introduction of EEI in any wide field or TIRF microscope. The additional benefits, EEI can bring, were illustrated by three test cases. Besides full frame hyperspectral imaging, it allows to record excitation spectra and hence create Stokes shift images. The latter can find application for imaging local heterogeneities that affect the Stokes shift, e.g. the polarity as illustrated for Nile Red in different matrices. In combination with optimized polarization optics our approach should also be realizable at the single molecule level where the nanoscopic environment leads to strong heterogeneities in the measured Stokes shift [22]. The presented approach can enhance the currently established hyperspectral imaging methods in the fields of life and materials science imaging.

References

1. J. R. Lakowicz, *Principles of fluorescence spectroscopy* (Springer, 2006).
2. B. Valeur and M. N. Berberan-Santos, *Molecular fluorescence: principles and applications* (John Wiley & Sons, 2012).
3. R. Arppe-Tabbara, M. R. Carro-Temboury, C. Hempel, T. Vosch, and T. J. Sørensen, "Luminescence from lanthanide (III) ions bound to the glycocalyx of Chinese hamster ovary cells," Chemistry **24**(46), 11885–11889 (2018).
4. Z. Liao, M. Tropiano, K. Mantulnikovs, S. Faulkner, T. Vosch, and T. Just Sørensen, "Spectrally resolved confocal microscopy using lanthanide centred near-IR emission," Chem. Commun. (Camb.) **51**(12), 2372–2375 (2015).
5. Y. Garini, I. T. Young, and G. McNamara, "Spectral imaging: principles and applications," Cytometry A **69A**(8), 735–747 (2006).
6. Z. Malik, D. Cabib, R. A. Buckwald, A. Talmi, Y. Garini, and S. G. Lipson, "Fourier transform multipixel spectroscopy for quantitative cytology," J. Microsc.-Oxford **182**(2), 133–140 (1996).
7. T. Zimmermann, J. Rietdorf, and R. Pepperkok, "Spectral imaging and its applications in live cell microscopy," FEBS Lett. **546**(1), 87–92 (2003).
8. R. Yan, S. Moon, S. J. Kenny, and K. Xu, "Spectrally resolved and functional super-resolution microscopy via ultrahigh-throughput single-molecule spectroscopy," Acc. Chem. Res. **51**(3), 697–705 (2018).
9. L. Gao, R. T. Kester, N. Hagen, and T. S. Tkaczyk, "Snapshot image mapping spectrometer (IMS) with high sampling density for hyperspectral microscopy," Opt. Express **18**(14), 14330–14344 (2010).
10. R. A. Schultz, T. Nielsen, J. R. Zavaleta, R. Ruch, R. Wyatt, and H. R. Garner, "Hyperspectral imaging: a novel approach for microscopic analysis," Cytometry **43**(4), 239–247 (2001).
11. H. Tsurui, H. Nishimura, S. Hattori, S. Hirose, K. Okumura, and T. Shirai, "Seven-color fluorescence imaging of tissue samples based on Fourier spectroscopy and singular value decomposition," J. Histochem. Cytochem. **48**(5), 653–662 (2000).
12. S. Moon, R. Yan, S. J. Kenny, Y. Shyu, L. Xiang, W. Li, and K. Xu, "Spectrally resolved, functional super-resolution microscopy reveals nanoscale compositional heterogeneity in live-cell membranes," J. Am. Chem. Soc. **139**(32), 10944–10947 (2017).
13. E. Schröck, S. du Manoir, T. Veldman, B. Schoell, J. Wienberg, M. A. Ferguson-Smith, Y. Ning, D. H. Ledbetter, I. Bar-Am, D. Soenksen, Y. Garini, and T. Ried, "Multicolor spectral karyotyping of human chromosomes," Science **273**(5274), 494–497 (1996).
14. M. R. Speicher, S. G. Ballard, and D. C. Ward, "Karyotyping human chromosomes by combinatorial multi-fluor FISH," Nat. Genet. **12**(4), 368–375 (1996).
15. W. Groner, J. W. Winkelman, A. G. Harris, C. Ince, G. J. Bouma, K. Messmer, and R. G. Nadeau, "Orthogonal polarization spectral imaging: A new method for study of the microcirculation," Nat. Med. **5**(10), 1209–1212 (1999).
16. I. Amenabar, S. Poly, M. Goikoetxea, W. Nuansing, P. Lasch, and R. Hillenbrand, "Hyperspectral infrared nanoimaging of organic samples based on Fourier transform infrared nanospectroscopy," Nat. Commun. **8**, 14402 (2017).
17. G. Lu and B. Fei, "Medical hyperspectral imaging: a review," J. Biomed. Opt. **19**(1), 10901 (2014).
18. Q. Li, X. He, Y. Wang, H. Liu, D. Xu, and F. Guo, "Review of spectral imaging technology in biomedical engineering: achievements and challenges," J. Biomed. Opt. **18**(10), 100901 (2013).
19. J. Dellinger, K. Van Do, X. Le Roux, F. De Fornel, E. Cassan, and B. Cluzel, "Hyperspectral optical near-field imaging: Looking graded photonic crystals and photonic metamaterials in color," Appl. Phys. Lett. **101**(14), 141108 (2012).
20. G. A. Roth, S. Tahiliani, N. M. Neu-Baker, and S. A. Brenner, "Hyperspectral microscopy as an analytical tool for nanomaterials," Wiley Interdiscip. Rev. Nanomed. Nanobiotechnol. **7**(4), 565–579 (2015).
21. D. Lepage, A. Jimenez, J. Beauvais, and J. J. Dubowski, "Conic hyperspectral dispersion mapping applied to semiconductor plasmonics," Light Sci. Appl. **1**(9), e28 (2012).
22. M. Streiter, S. Krause, C. von Borczyskowski, and C. Deibel, "Dynamics of single-molecule stokes shifts: Influence of conformation and environment," J. Phys. Chem. Lett. **7**(21), 4281–4284 (2016).
23. Q. Pian, R. Yao, N. Sinsuebphon, and X. Intes, "Compressive hyperspectral time-resolved wide-field fluorescence lifetime imaging," Nat. Photonics **11**(7), 411–414 (2017).
24. D. Melnikau, S. Elcoroaristizabal, and A. G. Ryder, "An excitation emission fluorescence lifetime spectrometer using a frequency doubled supercontinuum laser source," Methods Appl. Fluoresc. **6**(4), 045007 (2018).
25. L. Piatkowski, E. Gellings, and N. F. van Hulst, "Broadband single-molecule excitation spectroscopy," Nat. Commun. **7**(1), 10411 (2016).

26. P. F. Favreau, C. Hernandez, T. Heaster, D. F. Alvarez, T. C. Rich, P. Prabhat, and S. J. Leavesley, "Excitation-scanning hyperspectral imaging microscope," J. Biomed. Opt. **19**(4), 46010 (2014).

27. A. Perri, F. Preda, C. D'Andrea, E. Thyrhaug, G. Cerullo, D. Polli, and J. Hauer, "Excitation-emission Fourier-transform spectroscopy based on a birefringent interferometer," Opt. Express **25**(12), 483–490 (2017).

28. A. Perri, J. H. Gaida, A. Farina, F. Preda, D. Viola, M. Ballottari, J. Hauer, S. De Silvestri, C. D'Andrea, G. Cerullo, and D. Polli, "Time- and frequency-resolved fluorescence with a single TCSPC detector via a Fourier-transform approach," Opt. Express **26**(3), 2270–2279 (2018).

29. E. Thyrhaug, S. Krause, A. Perri, G. Cerullo, D. Polli, T. Vosch, and J. Hauer, "Single-molecule excitation-emission spectroscopy," Proc. Natl. Acad. Sci. U.S.A. (Accepted).

30. Y. Ma, M. R. Shortreed, and E. S. Yeung, "High-throughput single-molecule spectroscopy in free solution," Anal. Chem. **72**(19), 4640–4645 (2000).

31. S. R. Kirchner, K. W. Smith, B. S. Hoener, S. S. E. Collins, W. Wang, Y.-Y. Cai, C. Kinnear, H. Zhang, W.-S. Chang, P. Mulvaney, C. F. Landes, and S. Link, "Snapshot hyperspectral imaging (SHI) for revealing irreversible and heterogeneous plasmonic processes," J. Phys. Chem. C **122**(12), 6865–6875 (2018).

32. D. Brida, C. Manzoni, and G. Cerullo, "Phase-locked pulses for two-dimensional spectroscopy by a birefringent delay line," Opt. Lett. **37**(15), 3027–3029 (2012).

33. F. Preda, A. Oriana, J. Réhault, L. Lombardi, A. C. Ferrari, G. Cerullo, and D. Polli, "Linear and nonlinear spectroscopy by a common-path birefringent interferometer," IEEE J. Sel. Top. Quant. **23**(3), 88–96 (2017).

34. J. W. Brault, "High precision Fourier transform spectrometry: The critical role of phase corrections," Mikrochim. Acta **93**(1-6), 215–227 (1987).

35. N. de Oliveira, M. Roudjane, D. Joyeux, D. Phalippou, J.-C. Rodier, and L. Nahon, "High-resolution broad-bandwidth Fourier-transform absorption spectroscopy in the VUV range down to 40 nm," Nat. Photonics **5**(3), 149–153 (2011).

36. P. Greenspan and S. D. Fowler, "Spectrofluorometric studies of the lipid probe, Nile red," J. Lipid Res. **26**(7), 781–789 (1985).

37. A. Kawski, P. Bojarski, and B. Kukliński, "Estimation of ground- and excited-state dipole moments of Nile red dye from solvatochromic effect on absorption and fluorescence spectra," Chem. Phys. Lett. **463**(4-6), 410–412 (2008).

38. A. K. Dutta, K. Kamada, and K. Ohta, "Spectroscopic studies of Nile red in organic solvents and polymers," J. Photoch. Photobio. A **93**(1), 57–64 (1996).

39. H. Strahl, F. Bürmann, and L. W. Hamoen, "The actin homologue MreB organizes the bacterial cell membrane," Nat. Commun. **5**(1), 3442 (2014).

40. A.-Y. Jee, S. Park, H. Kwon, and M. Lee, "Excited state dynamics of Nile red in polymers," Chem. Phys. Lett. **477**(1-3), 112–115 (2009).

41. S. Krause, M. H. Overgaard, and T. Vosch, "Photon energy dependent micro-Raman spectroscopy with a continuum laser source," Sci. Rep. **8**(1), 11621 (2018).

42. Z. Liao, E. N. Hooley, L. Chen, S. Stappert, K. Müllen, and T. Vosch, "Green emitting photoproducts from terrylene diimide after red illumination," J. Am. Chem. Soc. **135**(51), 19180–19185 (2013).